Title

Engineered bone marrow as a clinically relevant ex vivo model for primary bone cancer research and drug screening

Journal

Proceedings of the National Academy of Sciences of the United States of America, 120(39)

ISSN

0027-8424

Authors

Griffin, Katherine H
Thorpe, Steven W
Sebastian, Aimy
et al.

Publication Date

2023-09-26

DOI

10.1073/pnas.2302101120

PNAS RESEARCH ARTICLE | MEDICAL SCIENCES ENGINEERING OPEN ACCESS

Engineered bone marrow as a clinically relevant ex vivo model for primary bone cancer research and drug screening

Katherine H. Griffin[a,b], Steven W. Thorpe[a], Aimy Sebastian[c], Nicholas R. Hum[c], Thomas P. Coonan[d], Isabel S. Sagheb[d], Gabriela G. Loots[a,c], R. Lor Randall[a], and J. Kent Leach[a,d,1]

Edited by David J. Mooney, Harvard University, Cambridge, MA; received February 7, 2023; accepted August 17, 2023 by Editorial Board Member Rakesh K. Jain

Osteosarcoma (OS) is the most common primary malignant bone cancer in children and adolescents. While numerous other cancers now have promising therapeutic advances, treatment options for OS have remained unchanged since the advent of standard chemotherapeutics and offer less than a 25% 5-y survival rate for those with metastatic disease. This dearth of clinical progress underscores a lack of understanding of OS progression and necessitates the study of this disease in an innovative system. Here, we adapt a previously described engineered bone marrow (eBM) construct for use as a three-dimensional platform to study how microenvironmental and immune factors affect OS tumor progression. We form eBM by implanting acellular bone-forming materials in mice and explanting the cellularized constructs after 8 wk for study. We interrogate the influence of the anatomical implantation site on eBM tissue quality, test ex vivo stability under normoxic (5% O_2) and standard (21% O_2) culture conditions, culture OS cells within these constructs, and compare them to human OS samples. We show that eBM stably recapitulates the composition of native bone marrow. OS cells exhibit differential behavior dependent on metastatic potential when cultured in eBM, thus mimicking in vivo conditions. Furthermore, we highlight the clinical applicability of eBM as a drug-screening platform through doxorubicin treatment and show that eBM confers a protective effect on OS cells that parallel clinical responses. Combined, this work presents eBM as a cellular construct that mimics the complex bone marrow environment that is useful for mechanistic bone cancer research and drug screening.

osteosarcoma | cancer | model | tumorigenesis | bone marrow

Osteosarcoma (OS) is the most common primary, malignant bone tumor in children and adolescents (1). Treatment options have varied little since the introduction of standard chemotherapies (e.g., doxorubicin, cisplatin, and methotrexate) in the 1970s (2–4). This underscores a critical need to better understand primary OS tumor biology, the events leading to pulmonary metastasis, and identify therapeutic targets to limit those events.

Current in vitro models fail to account for key components in OS biology, often overlooking the three-dimensional (3D) nature of sarcomas and OS tumor heterogeneity and microenvironment (5–10). Solid tumors possess an array of clinical and research challenges, from decreased drug penetration to alterations in cell-matrix cues and tumor cell mechanotransduction to poorly understood immune interactions and signaling. To interrogate some of these points, various groups have reported that OS 3D culture techniques, such as formation into spheroids or culture within a biomaterial, elicit altered behavior from monolayer culture (11–19). Other groups have investigated the interplay between hypoxia and OS (15, 20), attempted to simulate the bone marrow extracellular matrix (ECM) with hydroxyapatite (21–23), and demonstrated that 3D coculture with other stromal and progenitor cells can alter OS paracrine signaling to surrounding cells (24–27). While these studies provide insight into specific components that influence OS behavior, they currently have not yielded significant progress toward effective therapeutic targets in part due to the isolated nature of the interrogations. Because these studies fail to accurately mimic numerous integral components of the complex bone marrow environment in which OS originates, they exclude key cellular interactions involved in primary tumor formation and development. The complexity of OS mandates a combinatorial approach to modeling that accounts for multiple environmental variables.

Native bone marrow cannot be maintained in culture and is difficult to recapitulate in vitro, necessitating a reliance on in vivo experiments to attempt to overcome these limitations. Orthotopic intraosseous OS models are commonly used to study primary tumor biology and the events leading to metastasis (28–30). However, the draining tract between the bone marrow space and circulating vasculature renders the key events

Significance

The treatment of osteosarcoma (OS) and improvement of disease outcome has seen limited clinical progress due to a lack of understanding regarding primary and metastatic OS pathophysiology. Such improvements require improved understanding of the events leading from early OS development in the bone marrow to preferential pulmonary metastasis, yet limited models exist to investigate these events. The engineered bone marrow in this project accounts for the diverse cell population, complex cytokine assortment, and three-dimensional components of OS, thereby surpassing previous in vitro models that do not account for the combined effects of these key parameters. Here, we show its use in basic science research to study primary tumor formation, as well as its translational applications as a drug screening platform.

Author contributions: K.H.G., S.W.T., G.G.L., and J.K.L. designed research; K.H.G., A.S., N.R.H., T.P.C., and I.S.S. performed research; K.H.G., A.S., and G.G.L. analyzed data; J.K.L. supervision, administrative support; and K.H.G., S.W.T., G.G.L., R.L.R., and J.K.L. wrote the paper.

The authors declare no competing interest.

This article is a PNAS Direct Submission. D.J.M. is a guest editor invited by the Editorial Board.

[1]To whom correspondence may be addressed. Email: jkleach@ucdavis.edu.

This article contains supporting information online at https://www.pnas.org/lookup/suppl/doi:10.1073/pnas.2302101120/-/DCSupplemental.

of interest—the biological transition from primary to metastatic disease—irrelevant by bypassing the metastatic cascade and instead supplying OS with a direct, physical path to systemic circulation (31). These studies are also often performed using immunocompromised mice, which alters the hematopoietic niche and renders these models largely ineffective for the study of OS–bone marrow interactions (32). There are currently no models that combine crucial parameters of the bone marrow niche in which OS arises, such as the physiological oxygen tension, microarchitectural structure, and unique mixture of progenitor cells and cytokines (5, 33). Thus, there remains a critical lack of physiologically relevant models that reproduce the complex tumor biology in a biomimetic environment.

To address the gap between current models and clinical OS, we engineered an ex vivo bone marrow that enables direct investigation of primary tumor formation and progression. Modifying a technique described previously, we developed an engineered bone marrow (eBM) that recapitulates the native bone marrow niche in both microarchitecture and cellular composition (34). Here, we validate our model, demonstrate its use as a 3D platform to study bone cancer, and compare it to human clinical samples. We hypothesized that OS would exhibit tumorigenic and drug-resistant behavior that more accurately recapitulates the complexity of clinical disease when cultured in our physiologically relevant eBM compared to conventional tissue engineering techniques.

Results

Anatomical Implantation Site Influences eBM Quality. We investigated the influence of anatomical implantation site on eBM quality, comparing subcutaneous (as reported in ref. 34) with subfascial implantation. We chose to interrogate subfascial implantation as bone is naturally surrounded by muscle. Thus, we hypothesized that eBM formed subfascially could alter the morphology and cellular composition compared to subcutaneous formation. Grossly, subfascial eBM appeared better vascularized and generally more robust compared to the subcutaneous eBM (Fig. 1*B*). H&E (hematoxylin and eosin) staining of the cortical bone mirrored the findings of the gross images, revealing dense eosin staining and greater tissue deposition around the demineralized bone matrix (DBM) chips in the subfascial construct compared to the subcutaneous implant (Fig. 1*C*). Cross-sectional H&E staining revealed bone marrow niches surrounded by a cortical bone shell in samples from both sites, yet the bone marrow space in the subfascial eBM was considerably larger than in the subcutaneous eBM (Fig. 1*D*). In both groups, we also observed remaining DBM and surrounding fibrous tissue on one side of the marrow niche. Compared to an H&E-stained native mouse femur (S2), which features a thick cortical shell and dense bone marrow niche, the microarchitecture of the subfascial construct was more representative of the native environment. Cortical bone from subfascial eBM (Fig. 1 *E*, *Left*) exhibited less CD31 and osteocalcin (OCN) staining compared to subcutaneous (Fig. 1 *E*, *Right*). The increased CD31 and OCN staining in subcutaneous constructs indicates more bone formation consistent with active ectopic bone formation. These findings establish that eBM implantation in the subfascial site produces improved bone marrow tissue compared to subcutaneous implantation.

To further probe whether the subfascial eBM was forming ectopic bone or a robust hematopoietic niche, we increased the concentration of BMP-2 and BMP-4 10-fold to 33.3 μg/mL. Predictably, we observed rampant bone formation in these constructs compared to the normal eBM protocol. At the sites of implantation, eBM had fused with the underlying ribcage and pelvis (S3A). Furthermore, bone formation extended beyond the PDMS (polydimethylsiloxane) mold, often encasing it (S3B). Progenitor cell populations were evaluated via flow cytometry, which revealed that hematopoietic progenitor cells ($\mathrm{Lin}^{-}\mathrm{CD34}^{+}$) in eBM formed with the higher concentration of BMPs were significantly decreased compared to murine bone marrow and eBM formed with the lower concentration of BMPs (S3C). Additionally, OCN staining of the ectopic bone matched the cortical bone in a femur control, indicating significant osteogenesis and ectopic bone formation (S3D). These results demonstrate that increased BMP concentrations generate ectopic bone that has decreased capacity to support the hematopoietic niche.

We next analyzed the cell populations in subfascial eBM compared to native bone marrow with flow cytometry (Fig. 1 *F*–*H*). Native bone marrow was flushed from the femur of a healthy mouse not used for eBM synthesis and immediately stained with antibodies for flow cytometry as a control. Subfascial eBM was digested immediately after collection to form a single-cell suspension, then stained. Representative flow plots of lineage-restricted and nonrestricted cells in native bone marrow (Fig. 1*F*) and subfascial eBM (Fig. 1*G*) are closely mimicked, as evidenced by the general cell populations present. Furthermore, the number of lineage nonrestricted, or total progenitor cells, was statistically similar between native bone marrow and eBM (Fig. 1*H*). Together, these data establish that subfascial eBM synthesis improves tissue quality compared to subcutaneous implantation, resulting in a construct that closely mimics native bone marrow both microarchitecturally and cellularly.

The Anatomical Site of Implantation Does Not Influence Cellular Composition of eBM. We characterized subfascial eBM formed in cranial and caudal implantation sites to determine whether differences in thoracic and pelvic muscle mass and construct proximity to endogenous bone impacted eBM composition (S4A). To broadly identify the tissue composition, we stained eBM cross-sections with Masson's trichrome (MT) (S4B). This revealed a collagen-rich, cortical matrix surrounding a bone marrow niche in both the cranial and caudal eBMs. As noted previously, there is also remaining DBM and fibrous tissue on one side of the eBM.

With an eye toward ex vivo use, eBM was collected and maintained under dynamic culture in StemSpan serum-free expansion medium (SFEM) overnight to allow progenitor cell populations to stabilize. To further simulate the bone marrow niche, we also investigated the impact of ambient and physiological culture conditions (21% O_2 and 5% O_2, respectively) on eBM. To characterize cellular composition, we analyzed eBM progenitor cell populations with flow cytometry. Overall progenitor populations [lineage nonrestricted (Lin^{-} cells)] were statistically similar between cranial and caudal eBM at both oxygen tensions (S4C). The close interaction between hematopoietic stem cells (HSCs) and primary OS clearly influences disease emergence and progression, but HSCs have yet to be included in any in vitro models. Therefore, we also analyzed HSC subpopulations, $\mathrm{Lin}^{-}\mathrm{CD34}^{+}$ (S4D) and $\mathrm{Lin}^{-}\mathrm{cKit}^{+}\mathrm{Sca1}^{+}$ (S4E), which also revealed no differences between cranial and caudal locations or as a function of oxygen tension.

eBM Can be Maintained in Culture with Minimal Changes over Time. Having demonstrated similarities to native bone marrow and minimal variability between constructs, we sought to determine the potential of eBM for use as a cellular construct. We examined its stability and viability in culture over time by assessing eBM after 1 and 7 d in dynamic culture under 21% O_2 and 5% O_2 (Fig. 2*A*). Tissue quality and microarchitecture

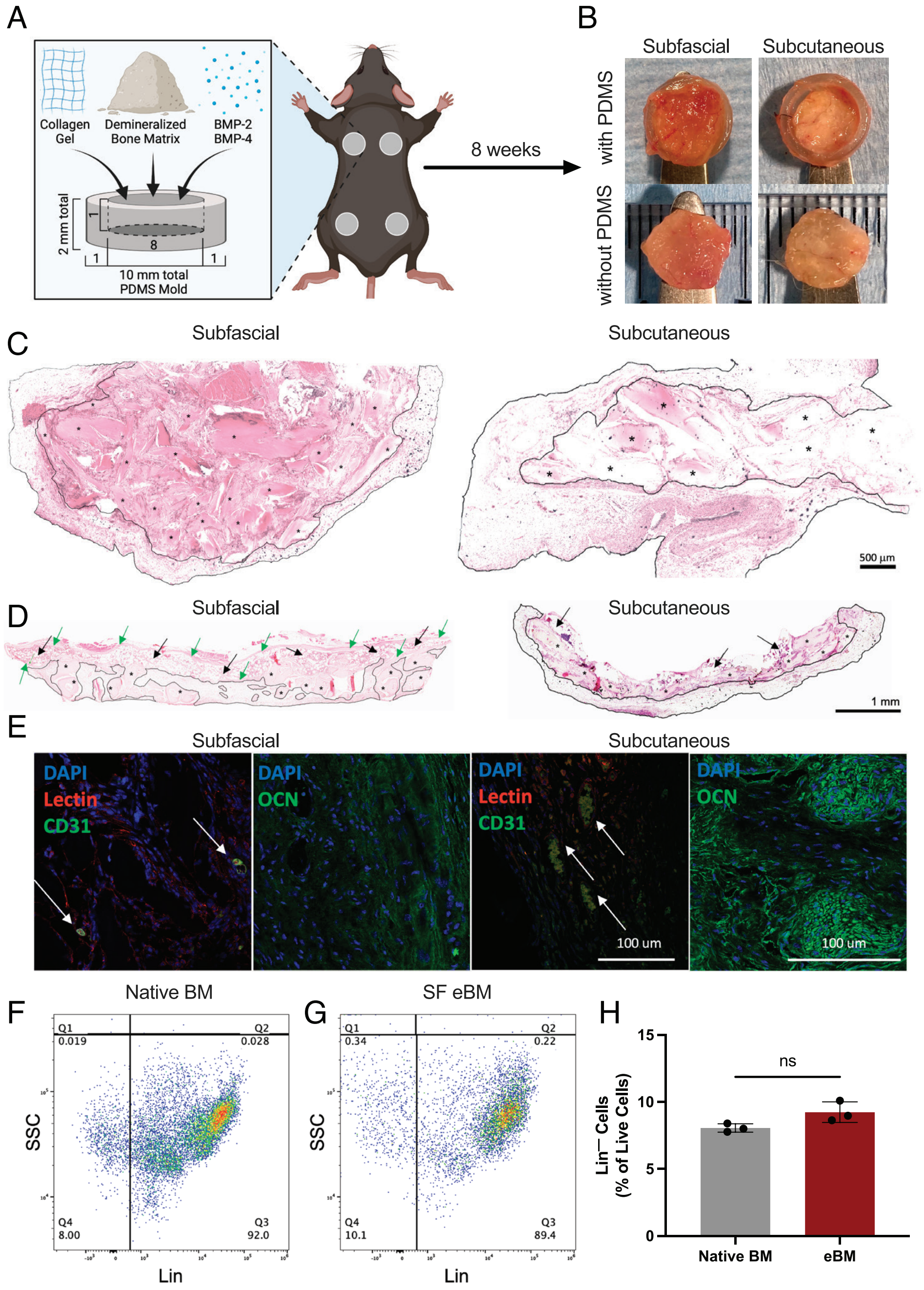

Fig. 1. Subfascial implantation yields eBM of improved quality compared to subcutaneous implantation. (*A*) Schematic of eBM construct synthesis. (*B*) Gross images of subfascial and subcutaneous eBM immediately after explantation. Representative H&E stains of eBM (*C*) cortical bone face and (*D*) cross-sections; asterisks denote DBM, fibrous tissue is outlined in black, black arrows denote marrow niche, green arrows denote cortical shell around marrow niche; (scale bars are 500 μm and 1 mm, respectively.) (*E*) CD31-lectin costaining (white arrows) and OCN staining of the cortical bone in subfascial (*Left*) and subcutaneous (*Right*) eBM, (scale bar is 100 μm.) Flow plots of lineage-restricted and nonrestricted cells in (*F*) native bone marrow and (*G*) subfascial eBM. (*H*) Quantification of lineage nonrestricted cells. Data are mean ± SD (n = 3); ns denotes no significance among all groups.

were consistent between time points when evaluated via MT staining (Fig. 2*B*). We used alamarBlue to determine metabolic activity, which remained constant after 1 wk in culture (Fig. 2*C*), indicating similar eBM viability and cellular function over time.

We also evaluated cellular changes in the bone marrow niche of the eBM. Although Lin$^-$ cells remained constant between both time points and culture conditions (Fig. 2*D*), analysis of HSC subpopulations revealed small changes under certain conditions. Lin$^-$CD34$^+$ cells decreased after 1 wk in culture, only at 21% O_2 (Fig. 2*E*, $P = 0.0051$), while Lin$^-$cKit$^+$Sca1$^+$ cells increased significantly only at 5% O_2 (Fig. 2*F*, $P < 0.0001$). Although these changes may add complexity to data interpretation, the change in Lin$^-$CD34$^+$ frequency is within the range of both time points of the 5% O_2 group, suggesting minimal functional impact on future studies under the same conditions. Further, the increase in Lin$^-$cKit$^+$Sca1$^+$ cells is expected with the use of SFEM media, as it is specifically formulated to support progenitor cell growth and survival. The differential behavior observed between oxygen tensions suggests that the physiologically relevant 5% O_2 is indeed facilitating accurate simulation of the native bone marrow niche. These data demonstrate that we successfully maintained eBM in culture such that cellular and microarchitectural components remain intact.

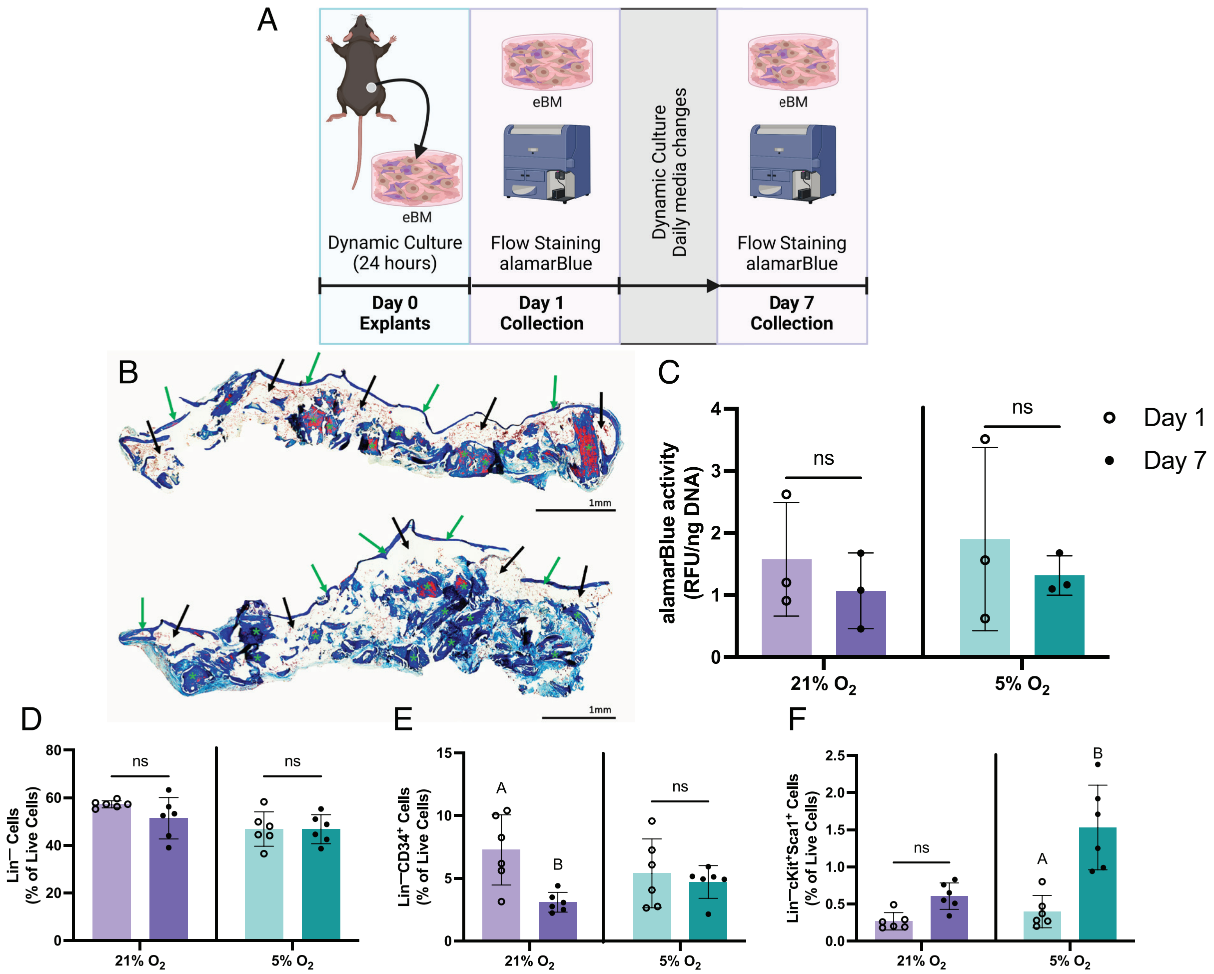

Fig. 2. eBM can be maintained in culture over time. (*A*) Schematic overview of experimental design and methods. (*B*) MT staining of eBM cross-sections after 1 (*Top*) and 7 d (*Bottom*) in culture; green asterisks denote DBM, black arrows denote marrow niche, and green arrows denote cortical shell around marrow niche; (scale bar is 1 mm.) (*C*) Quantification of alamarBlue activity, normalized to DNA, as an indicator of metabolic activity. Quantification of (*D*) Lin$^-$, (*E*) Lin$^-$CD34$^+$, and (*F*) Lin$^-$cKit$^+$Sca1$^+$ progenitor cells via flow cytometry. All data were analyzed after 1 and 7 d in dynamic culture in StemSpan SFEM media at 21% O_2 and 5% O_2. Data are mean ± SD (n = 3 to 6). Groups with statistically significant differences do not share the same letters; ns denotes no significance among groups.

OS Cell Lines in eBM Exhibit Distinct Behavior Based on Metastatic Potential. To assess eBM utility as a model for OS, we loaded eBM via direct injection with a highly metastatic OS cell line (K7M2), less metastatic OS cell line (K12), or nonmalignant preosteoblast control cell line (MC3T3). Cells were stained with CellTrace Yellow prior to loading for later identification. We maintained loaded eBM for up to 7 d in dynamic culture in StemSpan SFEM media at 21% O_2 and 5% O_2 (Fig. 3*A*). Upon collection, eBM was digested into a single-cell suspension, stained for flow cytometry, and analyzed. Under 21% O_2, MC3T3 and K12 cell populations were maintained between 1 and 7 d in culture, whereas K7M2 cells decreased over time (P = 0.0072). The same statistical trends were noted at 5% O_2, but the decrease in K7M2 cells was more pronounced ($P < 0.0001$) (Fig. 3*B*). These observations reflect cell line classifications and in vivo findings, where K7M2 cells are highly metastatic and K12 cells are less or nonmetastatic (35). K12s appear to remain in the eBM, but K7M2 cells may egress or are unsupported in the bone marrow environment.

The hematopoietic capacity of this eBM model also offers a unique opportunity to evaluate complex endogenous immune cell responses. Macrophages play a key role in shaping the OS tumor microenvironment (36, 37). Clinical data suggest that macrophage infiltration may correlate with OS outcome (38), yet the role of macrophage phenotype has only been rudimentarily characterized with histology and immunohistochemistry. Tumor-associated macrophages with an M2 phenotype are generally considered tumor-promoting (36), yet mechanistic in vitro studies are hindered by the previously described limitations (18, 39–42). Here, we evaluated endogenous macrophage response within eBM, specifically characterizing the total macrophage population, as well as M1- and M2-polarized macrophages (S5). We did not observe any significant changes in total macrophages (F4/80$^+$) or M2 polarized macrophages (F4/80$^+$CD206$^+$) between time points, oxygen tensions, or loaded samples (S5A and 5C, respectively). M1 macrophages (F/480$^+$CD86$^+$) increased significantly in eBM loaded with K7M2s at 21% O_2 after 7 d (S5B). At 5% O_2, there was also an increasing trend though not statistically significant. These data could, in part, account for the significant decrease we observed in K7M2s after 1 wk in culture, as M1 macrophages are considered tumor-inhibiting.

K12-Loaded eBM Exhibits the Greatest Inflammatory Cytokine Profile. The rich cytokine milieu is a key characteristic of the bone marrow niche. To further understand the soluble signaling within eBM, as well as the dynamic changes it undergoes with OS cell loading, we performed a multiplex protein analysis of the eBM media after 1 and 7 d in culture (Fig. 4). eBM alone featured a

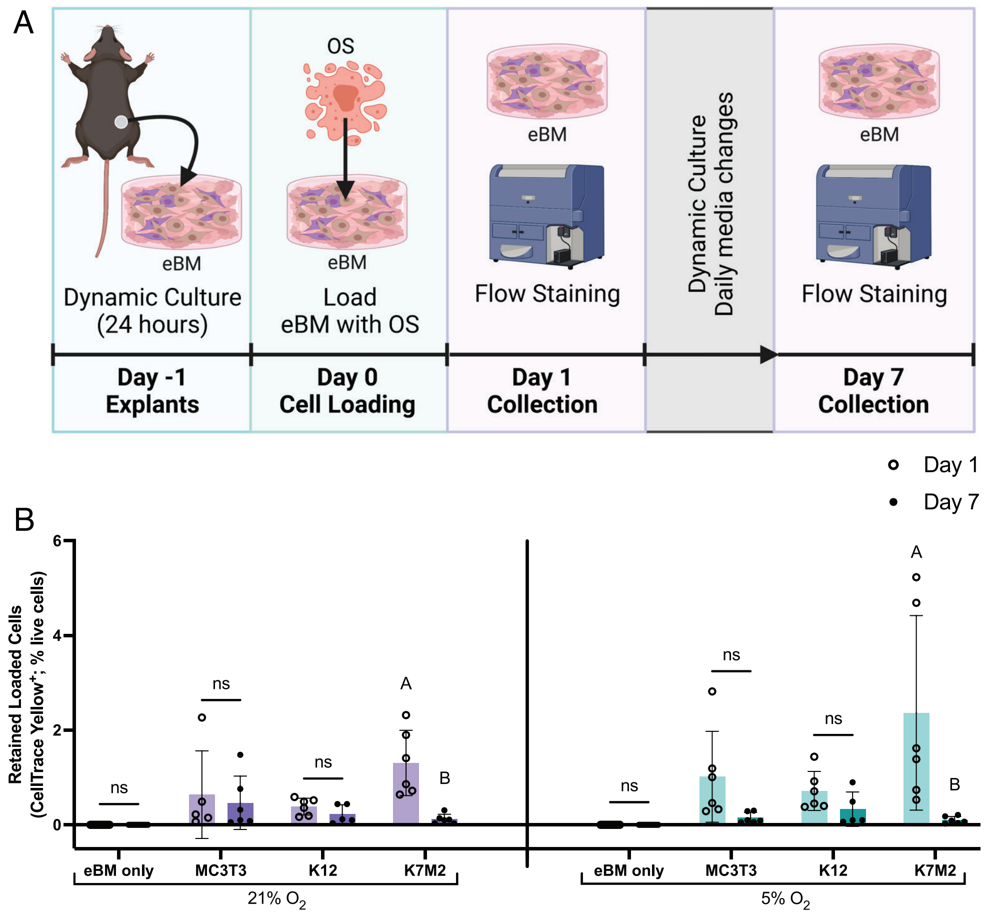

Fig. 3. OS cell lines in eBM exhibit differential behavior dependent on metastatic potential. (*A*) Schematic overview of experimental design and methods. (*B*) Quantification of loaded cells (MC3T3, K12, and K7M2 cells) via flow cytometry after 1 and 7 d under dynamic culture in StemSpan SFEM media at 21% O_2 and 5% O_2. Cells were identified as the CellTrace Yellow$^+$ population. Data are mean ± SD (n = 5 to 6). Groups with statistically significant differences do not share the same letters; ns denotes no significance among groups.

complex assortment of cytokines that exhibited a relative decrease over time, possibly indicating a stabilization in secreted factors after 7 d in culture.

Under both oxygen tensions, K12s induced the greatest cytokine upregulation when injected into eBM, featuring increased secretion of multiple inflammatory cytokines and chemokines. For example,

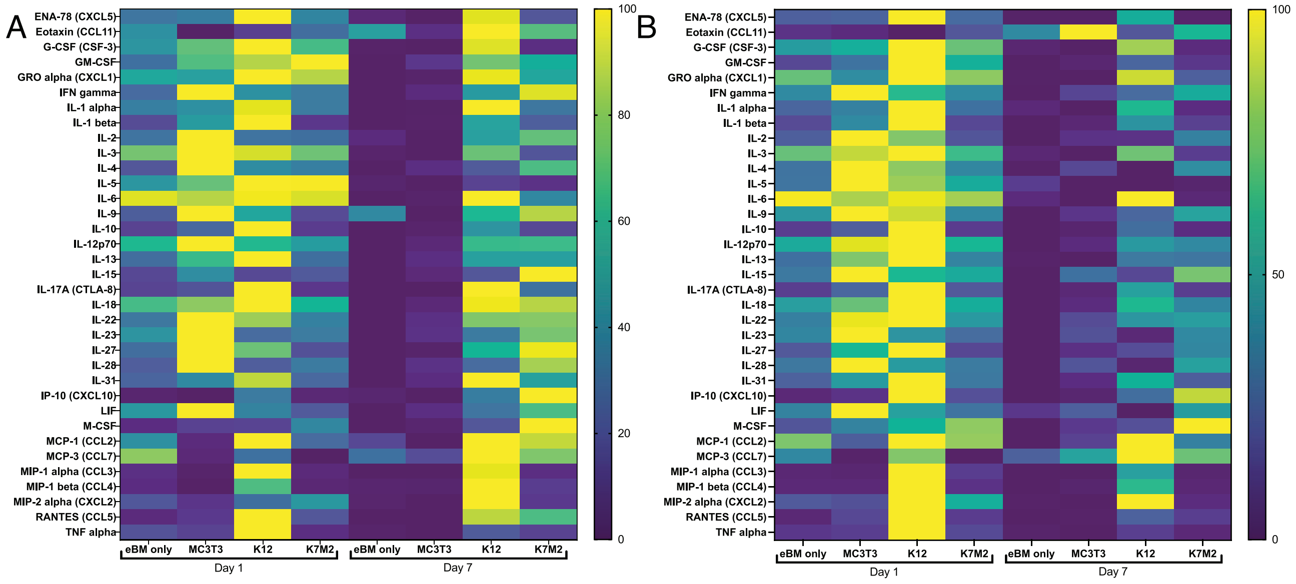

Fig. 4. eBM loaded with K12 cells exhibit the greatest upregulation in inflammatory cytokines. Multiplex proteomic analyses of eBM or eBM loaded with MC3T3, K12, or K7M2 cells after 1 and 7 d in culture under 21% (*A*) and 5% (*B*) O_2. n = 3 to 5, data are presented as mean and are normalized per analyte to a percentile scale where the lowest value is zero and the highest is 100.

IL-6 secretion increased slightly between 1 and 7 d in culture under 21% O_2 (21.3 ± 3.3 ng/mL to 21.7 ± 3.8 ng/mL, respectively) and 5% O_2 (25.6 ± 1.8 ng/mL to 26.5 ± 0.2 ng/mL, respectively). CCL2 exhibited a similar trend. Other inflammatory factors, such as IL-1α and CTLA-8, exhibited sustained secretion only at 21% O_2, whereas constructs in 5% O_2 had elevated levels at Day 1 but decreased by day 7. Other factors such as TNFa and IL-1β also had decreasing trends over time, but these trends were similar between oxygen tensions. Surprisingly, we did not detect the same level of inflammatory factor secretion for K7M2 cells, despite their categorization as a more aggressive cell line.

Cytokine profiling for eBM loaded with MC3T3 and K7M2 cells also revealed interesting trends. Generally, MC3T3-loaded eBM cultured under both oxygen tensions exhibited a downregulation in secreted factors over time but a relative upregulation in those loaded with K7M2 cells. These results are consistent with the macrophage polarization results (S4), and possibly indicate that noncancerous MC3T3 cells may reach an equilibrium within the constructs, consistent with the flow cytometry data (Fig. 4). However, K7M2s exhibit increased inflammatory signals between 1 and 7 d compared to the other groups, thus providing another possible mechanism for their decrease in the eBM constructs over time.

OS Cell Lines in eBM are Resistant to Doxorubicin. We investigated the potential of eBM for use as an improved anticancer drug screening platform. We compared OS in eBM with monolayer and 3D Matrigel culture, the two leading industry methods for therapeutic response experiments (Fig. 5*A*). All groups were cultured with constant doxorubicin exposure for 1 wk in 21% O_2 and 5% O_2.

Monolayer groups were seeded at confluency, then treated with 0 to 10 μM doxorubicin. After 7 d, DNA content was quantified as an indicator for cell number (Fig. 5 *B*–*D*). Doxorubicin dose and cell number were inversely related across all cell types and culture conditions. However, cell number was decreased across all cell types in 5% O_2 compared to culture at 21% O_2. While K7M2 and K12 cells exhibited similar cell numbers, MC3T3 cells were considerably lower, as expected. Doxorubicin treatment at 0.1 μM and 1 μM resulted in consistent, statistically significant decreases compared to untreated cells, motivating our study of those doses alone.

Matrigel constructs were loaded with 1 × 10^6 cells/mL of each cell type and then treated with doxorubicin at 0.1 μM and 1 μM. After 7 d, DNA content was again quantified as an indicator for cell number (Fig. 5 *E*–*G*). MC3T3 cells at 21% O_2 behaved similarly to monolayer culture, with significant decreases in DNA with doxorubicin treatment compared to untreated cells. However, we did not detect significant differences in cell number between treated and untreated cells at 5% O_2 (Fig. 5*E*). K12 cells demonstrated consistent decreases in DNA in treated vs. untreated groups across oxygen tensions, but unlike in monolayer culture, 3D culture in Matrigel rendered K12s less responsive to increased

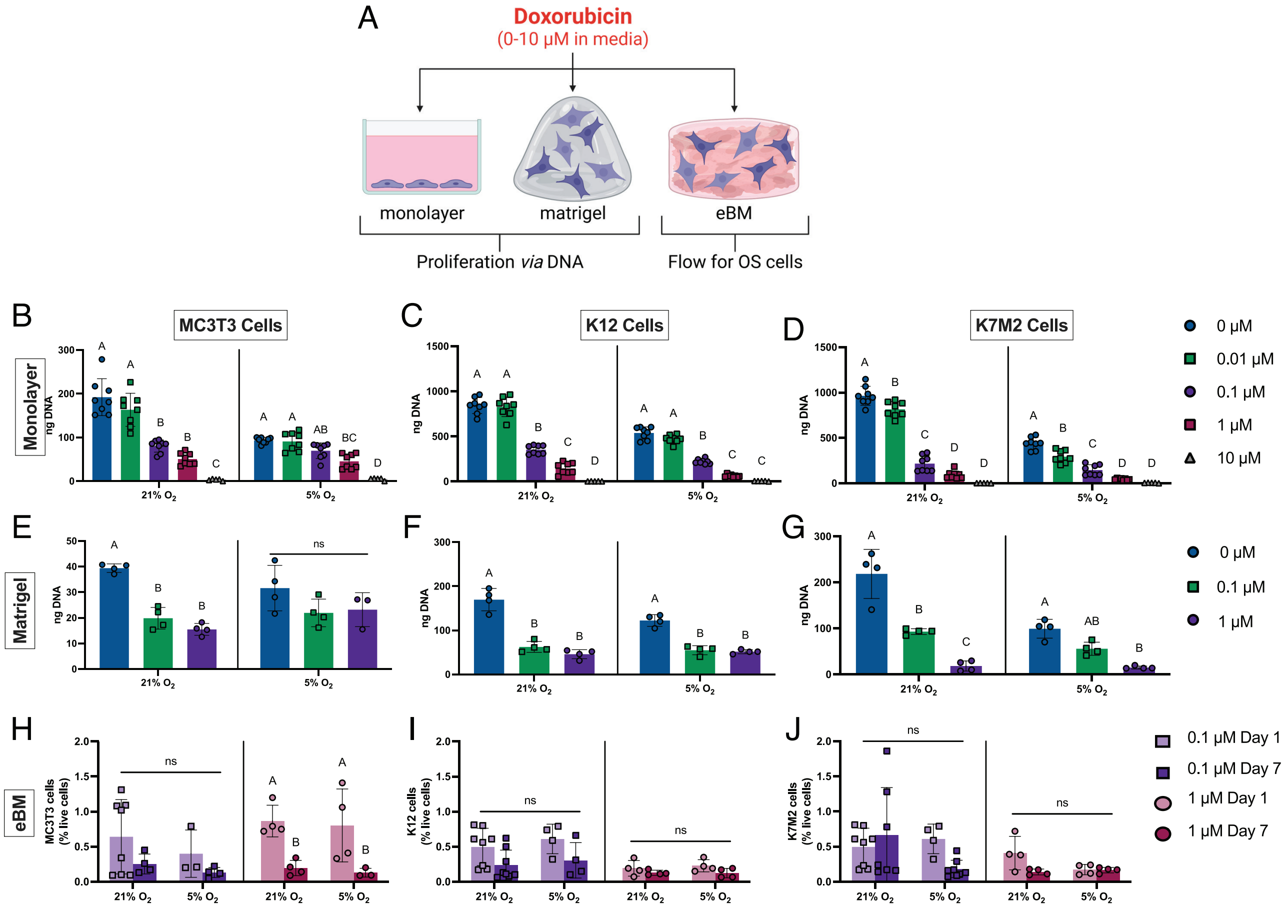

Fig. 5. OS cell lines cultured in eBM are resistant to doxorubicin treatment compared to typical drug screening models. (*A*) Schematic overview of experimental design and methods. Quantification of DNA content of MC3T3, K12, and K7M2 cells cultured in (*B*–*D*) monolayer or in (*E*–*G*) 3D Matrigel at 21% O_2 and 5% O_2 after 7 d with consistent exposure to 0 to 10 μM doxorubicin. (*H*–*J*) Quantification of loaded cells (MC3T3, K12, and K7M2 cells) in eBM via flow cytometry after 1 and 7 d in dynamic culture in StemSpan SFEM media with constant 0.1 to 1 μM doxorubicin at 21% O_2 and 5% O_2. Data are mean ± SD (n = 3 to 8). Groups with statistically significant differences do not share the same letters; ns denotes no significance among groups.

doxorubicin doses (Fig. 5*F*). Last, K7M2 cells in Matrigel had the same trends as monolayer culture across all conditions (Fig. 5*G*). Of note, similar trends in DNA content between oxygen tensions and cell types were generally still maintained in Matrigel culture. Therefore, while 3D culture in Matrigel elucidates some behavioral changes that are potentially useful for specific mechanistic investigations, it is still an oversimplified model that does not accurately mimic clinical disease or response to therapeutics.

eBM was loaded with MC3T3, K12, and K7M2 cells and treated with doxorubicin at 0.1 μM and 1 μM. After 1 and 7 d in dynamic culture, eBM was digested into a single-cell suspension, stained for flow cytometry, and analyzed (Fig. 5 *H*–*J*). Cells were considerably less susceptible to doxorubicin treatment when cultured in eBM compared to monolayer and Matrigel. MC3T3 cells in eBM did not significantly decrease over time when treated with 0.1 μM doxorubicin but decreased when treated with 1 μM (Fig. 5*H*). K12 cells cultured in eBM did not decrease over time regardless of dose. However, the number of K12 cells was generally decreased after 1 d when treated with 1 μM doxorubicin compared to 0.1 μM ($P = 0.069$ for 21% O_2, $P = 0.044$ for 5% O_2) (Fig. 5*I*). K7M2 cells cultured in eBM also did not significantly decrease over time when treated with either dose. However, culture in 5% O_2 resulted in stronger dose–response trends compared to 21% O_2. Specifically, 0.1 μM doxorubicin treatment at 5% O_2 reduced K7M2 number more over time ($P = 0.157$) compared to cells in 21% O_2 ($P = 0.762$). Overall, these data show that the complex microenvironment of the eBM confers a protective effect on OS cell lines.

We characterized endogenous macrophage populations in eBM treated with 0.1 μM and 1 μM doxorubicin (S6). Total macrophages (F4/80$^+$) decreased significantly between day 1 and day 7, but only under 0.1 μM treatment (S6A). Further M1 macrophages (F/480$^+$CD86$^+$) largely did not change, except for a decrease under 0.1 μM treatment at 21% O_2 (S6B). M2 macrophages (F/480$^+$CD206$^+$) consistently decreased across both doses and oxygen tensions (S6C). These data may indicate that doxorubicin eliminates shorter-lived immune cells, creating a niche for OS to persist, but there are clearly complex immune–OS–chemotherapeutic interactions that warrant further investigation beyond the scope of these studies.

To decouple the direct effect of doxorubicin on loaded OS vs. its effect on the hematopoietic niche and resultant influences on OS, we evaluated the HSC population in eBM treated with doxorubicin (S7). We did not detect differences in the frequency of HSCs (Lin$^-$cKit$^+$Sca1$^+$) in eBM treated with 0 to 1 μM doxorubicin in either oxygen tension after 7 d. Furthermore, HSCs remained constant at these doses when loaded with K7M2s, suggesting that immune cell changes due to OS behavior and response to chemotherapeutics do not tax the early stages of hematopoiesis to an extent that causes significant HSC proliferation. However, there was a decrease in HSCs when treated with 10 μM doxorubicin.

K7M2 Cells in eBM Exhibit Gene Expression Consistent with Human OS. We performed bulk RNA sequencing (RNA-seq) to interrogate the ability of eBM to recapitulate the complex signaling pathways of both bone and the OS tumor microenvironment. Because we only sought to understand whether eBM was capable of mimicking these complex niches, we studied eBM only, eBM loaded with K7M2 cells, and eBM + K7M2 cells treated with 0.1 μM doxorubicin. Following culture for 7 d at 21% O_2, we collected the constructs for RNA isolation and subsequent sequencing (Fig. 6*A*). Initial principal component analysis revealed distinct clustering of eBM only from eBM loaded with K7M2 cells (Fig. 6*B*).

To further explore differences in eBM only and OS-loaded eBM, we next identified differentially expressed genes, organized them according to biological process or signaling pathway, and presented them as heatmaps (Fig. 6 *C*–*F*). Unsurprisingly, we saw increases in pathways associated with proliferation (e.g., *Plk1* and *Ccnd1*) and metabolic function (Fig. 6 *D* and *E* and *SI Appendix*, Fig. S8*A*) in eBM loaded with K7M2 cells compared to eBM only. Congruent with the literature (43–45), we also found significant upregulation of genes associated with bone mineralization (e.g., *Bmp4*, *Wnt4*, *Wnt10b*, and *Osr2*) and interferon signaling (Fig. 6 *C* and *F* and *SI Appendix*, Fig. S8 *B*–*D*).

We also compared eBM to previously published human OS RNA-seq data (GEO number: GSE99671) that compares normal bone samples to OS (46). Differentially expressed homologous genes were similar between loaded eBM and human OS in numerous genes. Of those, many correlated with hallmarks of OS, such as the downregulation of neutrophil-associated genes (47) and reactive oxygen species regulation (48, 49), as well as the upregulation of myeloid lineage cells and signaling (50, 51), proliferation and ECM deposition (52), and hypoxia-induced factors (49, 53) (Fig. 6 *G*–*J* and *SI Appendix*, Fig. S9). These similarities between human samples and our eBM underscore the validity of eBM as a highly rigorous model of OS.

We sought to conclusively demonstrate the clinical relevance of this model by interrogating changes in gene expression in loaded eBM treated with doxorubicin (Fig. 6*K*). Compared to untreated eBM loaded with K7M2 cells, we did not observe stark differences in most genes with the exception of significantly down-regulated cell cycle-associated genes. Given the mechanism of action of doxorubicin, this is not surprising and further validates the utility of the model as a drug screening platform.

Discussion

Current in vitro models do not recapitulate the cellular and microarchitectural complexity of the native bone marrow environment in which OS arises. This lack of relevant biomimetic models is a key limitation in the identification and development of improved therapeutics that have been absent for decades. To address this challenge, we developed an eBM that closely mimics the hematopoietic niche, can be maintained in culture, and can support OS culture. This study introduces a fully cellular construct with physiologically accurate matrix cues, cellular organization, and cytokine signaling applied for the study of bone cancer tumorigenesis and drug screening. Our results reveal that OS tumorigenic behavior more accurately represents clinical disease when cultured in eBM compared to common methods in cancer research, namely culture in monolayer or Matrigel. Specifically, our data demonstrate that eBM hosts a complex cytokine milieu, faithfully mimics the gene expression profile of the human OS tumor microenvironment, and promotes OS resistance to doxorubicin treatment. These findings collectively demonstrate that the intercellular and environmental cues of bone marrow are integral to understanding clinical OS biology, tumorigenesis, and the events leading to metastasis.

As a platform for cancer research, the consensus between our flow cytometry, cytokine profiling, and gene expression analyses is a powerful indicator of the rigor of our model. For example, we observed significant decreases in K7M2 cells over time under both oxygen tensions, which is congruent with the relative increases in inflammatory cytokine signaling and up-regulated

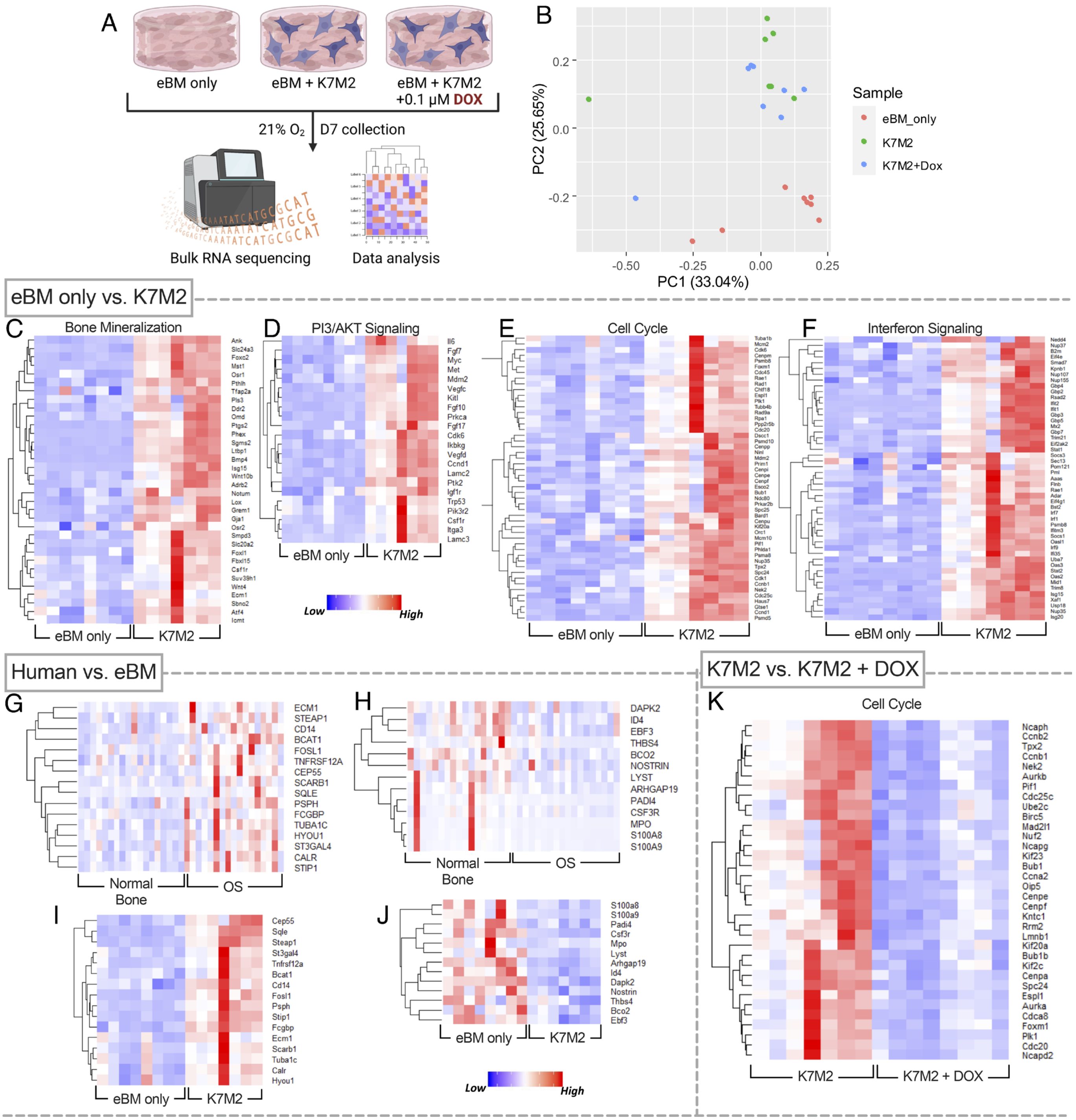

Fig. 6. RNA-seq of eBM loaded with K7M2 cells reveals gene expression behavior consistent with human OS. (*A*) Schematic overview of experimental design and methods. (*B*) Principal component analysis of eBM only, eBM loaded with K7M2 cells, and eBM+K7M2 cells treated with 0.1 µM doxorubicin (DOX). (*C*–*F*) Heatmaps representing RNA-seq data of differentially expressed genes associated with bone mineralization (*C*), PI3/AKT signaling (*D*), cell cycle (*E*), and interferon signaling (*F*) in eBM only compared to eBM loaded with K7M2 cells. (*G*–*J*) Heatmaps of differentially expressed genes in normal bone compared to OS samples in humans (*G* and *H*, GEO number: GSE99671) and homologous genes in eBM only and K7M2-loaded samples (*I* and *J*). (*K*) Heatmap of cell cycle genes that are down-regulated in eBM loaded with K7M2 cells treated with DOX. n = 17 for human samples and n = 7 to 8 for eBM.

interferon gene expression. This demonstrates a clear progression from the gene to protein to functional cellular response, which, given the increased cellular complexity of the model, highlights its utility and accuracy. Although we used RNA-seq as a validation assay, future studies could afford in-depth analyses of OS tumor development and progression on a level currently unachievable in the clinic. Even with our limited groups, we noted intricacies in overlapping gene expression that would be exceedingly challenging to decipher in primary tumors. For example, we detected divergent *Wnt* expression in K7M2-loaded eBM (S8B and D). Genes associated with predominantly canonical *Wnt* were up-regulated, which correlates with up-regulated proliferation from the PI3/AKT and cell cycle heatmaps, whereas noncanonical *Wnt* genes were down-regulated, which is consistent with the significant downregulation of calcium signaling (S8C) (54, 55).

The combination of collagen and BMPs for bone formation is well characterized and has been used for translational tissue engineering studies for decades (34, 56, 57). However, employing these traditionally in vivo strategies with the intent for explantation and ex vivo use is uncommon (34). As a cellularized model, eBM provides remarkable potential as a bridge between in vivo complexity and in vitro control and tunability. We and others have characterized the diverse cell populations and environmental niches within eBM (34). Though unexplored here, we speculate that these populations can be altered via depletion or inhibition during eBM formation, enabling further investigation of the roles of each cell type in hematopoiesis, tumor formation, or other biological processes. Compared to previous work (34), the size of eBM is adjustable depending on the needs of the study. The tunability of in vitro culture conditions provides further flexibility and manipulation of this system, as demonstrated by culture in different oxygen tensions. Together, these points highlight how our platform could overcome the shortcomings of other in vitro models and the challenges associated with recapitulating the bone marrow environment.

Developments in cancer therapeutics, particularly immunotherapies, have substantially improved treatment options for certain highly prevalent cancers, such as melanoma, leukemia, and breast cancer (58, 59). However, patients with sarcomas are broadly unaffected by these advancements due to tumor heterogeneity, lack of immune microenvironment characterization, and a highly dense fibrous network that frequently inhibits therapeutic cell infiltration (2, 3, 58). OS remains an especially challenging tumor, often refractory to both experimental and traditional therapeutics (2, 3). Moreover, these patterns are seldom observed in vitro with the standard techniques of cancer research, such as culture in monolayer or 3D culture in a biomaterial (9, 60). This study offers a compelling demonstration of eBM as a clinically relevant platform for drug screening and the stark difference in OS cell susceptibility within eBM. Drug screening and pharmacodynamic studies undertaken in advanced model systems could accelerate downstream preclinical and clinical drug testing, further amplifying the advantages of eBM. Due to the intact hematopoietic niche and our characterization of the endogenous immune landscape, we also show that eBM has the potential to help identify targets for immunotherapies that may be more relevant to sarcomas. Our investigation of endogenous macrophage populations uncovered an intricate interplay between OS cells, macrophages, and doxorubicin within the eBM system that warrants further investigation beyond the scope of this paper. However, our data underscore that eBM supports endogenous macrophage culture over time, with no significant changes in total or polarized populations (S5), and that eBM can facilitate the study of tumor-immune cell interactions in a controlled system. These findings enable an increased understanding of OS tumorigenesis and the identification of therapeutic targets. In combination, this work confirms that eBM reveals more complex cancer biology than conventional culture techniques, which will provide valuable opportunities for pharmacodynamic analysis, high-throughput drug screening, and therapeutic target research.

Although the complexity and innovation of eBM yields a platform that offers significant advantages over current approaches used to study bone cancers, there are limitations to the use and translational applicability of the work. Of primary relevance to the clinic, species restrictions are an obvious challenge. The studies shown here are within a system in which complex interactions between OS cells and endogenous progenitor and immune cells are preserved. However, studying the intricacies of those interactions for primary tumors in human patients within the context of this platform is currently not possible. With an intact endogenous immune system in the eBM, xenogeneic investigations would deteriorate quickly. Humanized mice present a tempting solution but remain suboptimal due to incongruities between murine stromal cells and human hematopoiesis. For example, human monocytes and macrophages do not differentiate with murine macrophage colony-stimulating factor (M-CSF), thus missing a critical cue in macrophage lineages and development (61). A possible alternative is utilization of a canine model, which would represent an allogeneic application. Canine OS is largely considered to be a naturally occurring, highly prevalent model of the human disease (62), so this may provide the opportunity for further application of eBM with primary patient samples. Another limitation is the 8-wk-long in vivo development required for these constructs. Torisawa et al. showed that 4 wk was insufficient to generate high-quality bone marrow (34), so this remains a fixed restraint for eBM use. Lastly, the cortical shell of the eBM is necessary to form the interior hematopoietic niche; however, it creates substantial limitations to imaging these constructs. MicroCT can be used to characterize the mineralized components, and positron emission tomography can roughly identify areas of high metabolic activity, but direct, high-resolution, live cell imaging of the interior niche remains elusive. Though formidable, these limitations do not negate the benefits of an accurate, in vitro hematopoietic niche.

The drug dose–response data described here faces a major limitation in that it fails to account for replicative cell differences across culture platforms and cell types. However, current regression analysis metrics, such as GR_{50} calculations, cannot accurately model drug dose–response when the cell type of interest is not within the growth phase, as in our eBM (63). Therefore, new pharmacodynamic analysis techniques must be developed for application toward models with increased complexity where cellular response may be confounded by intact immune systems, infection, comorbidities, etc., to accurately normalize cell replication and behavior. This is outside the scope of this paper and requires further investigation before this model can be faithfully used as a drug screening platform.

Recognizing that in vivo models also have significant limitations, these studies have established eBM as an exciting platform that provides a significant advancement to in vitro primary bone tumor research, as well as biomaterial tissue engineering at large. Within the context of cancer, eBM has the potential to be used to study experimental cancer therapeutics, complex immune cell-cancer interactions, and metastagenesis biology, both as it relates to primary sarcoma metastasis away from bone and metastatic carcinoma to the bone. Data from this work clearly show that eBM provides significant cellular and microarchitectural advantages over traditional cancer research techniques, offering opportunities for impactful advances in our understanding of cancer biology and a potential platform for therapeutic testing.

Materials and Methods

eBM Synthesis and Culture. All animal studies were conducted in accordance with UC Davis animal care guidelines and all NIH animal handling procedures. eBM was produced in mice over 8 wk using an established protocol (34). Acellular constructs consisting of 10% (w/v) DBM (Arthrex), 3.3 to 33.3 μg/mL human recombinant bone morphogenetic proteins 2 and 4 (BMP-2 and BMP-4, Peprotech, Cranbury, NJ), and 3 mg/mL type I collagen gel (Advanced BioMatrix, Carlsbad, CA) were combined in 10 mm × 1 mm PDMS molds, which were sterilized in 70% ethanol for at least 24 h prior to use (*SI Appendix*, Fig. S1 and Fig. 1*A*). Gels were cross-linked for 1 h at 37 °C and then immediately implanted.

Male C57BL/6 mice (Jackson Laboratories, West Sacramento, CA) aged 10 to 12 wk were anesthetized and maintained with isoflurane through a nose cone. Each animal received four subcutaneous or subfascial implants (Fig. 1*A*). Following a dorsal midline incision, constructs in PDMS molds were placed subcutaneously with the open face of the construct down and sutured in place. For subfascial groups, fascia was incised, and blunt dissection was performed between the fascia and muscle belly. Constructs were again placed face-down on the muscle, sutured in place with 4-0 Monocryl sutures (Ethicon, Cornelia, GA), and the fascia and skin closed. After 8 wk, mice were killed, and eBM was collected and removed from PDMS. eBM was either characterized immediately or bisected and maintained on an orbital shaker under ambient and physiologic culture conditions (21% and 5% O_2, respectively) in StemSpan SFEM media (StemCell Technologies, Vancouver, BC Canada) to support the complex hematopoietic cell populations.

Cell Culture. Highly metastatic OS (K7M2, ATCC, Manassas, VA), less metastatic OS (K12, courtesy of Dr. Kurt Weiss, University of Pittsburgh Medical Center), and noncancerous preosteoblast controls (MC3T3-E1 subclone 4, ATCC) were cultured under standard and physiologic culture conditions. K7M2 and K12 cells were cultured in DMEM while MC3T3s were cultured in αMEM (both from Invitrogen, Carlsbad, CA). All media were supplemented with 10% fetal bovine serum (FBS) (Bio-Techne, Minneapolis, MN) and 1% penicillin–streptomycin (Gemini Bio Products, West Sacramento, CA). K7M2 cells were used when cells reached 60 to 70% confluency between passage 20 to 27; K12 cells were used when cells reached 60 to 70% confluency between passage 27 to 33; and MC3T3 cells were used when cells reached 80-90% confluency between passage 22 to 29.

Matrigel Loading. K7M2, K12, and MC3T3 cells were trypsinized and loaded into Growth Factor Reduced Matrigel (#354230, Corning, Bedford, MA) at 1×10^6 cells/mL as described (64, 65). Briefly, cells were pelleted *via* centrifugation at 250 g for 8 min at 4 °C and then resuspended on ice in Matrigel. Fifty microliters of cell suspension was then pipetted into cold v-bottom 96-well plates and allowed to cross-link at 37 °C for 1 h, after which 200 μL of the appropriate media was gently added to each well.

eBM Loading. Following explantation, eBM was kept in dynamic culture overnight to allow cell populations to stabilize in SFEM. K7M2, K12, and MC3T3 cells were trypsinized, stained with 5 μM CellTrace Yellow (Invitrogen) in phosphate buffered saline (PBS), and loaded at 250,000 cells per eBM *via* injection with a 22-G needle directly into the bone marrow portion of the eBM. eBM was returned to static culture for 1.5 h to allow cells to adhere. After seeding, media were refreshed, and eBM was returned to dynamic culture on an orbital shaker (Belly Dancer, Stovall, Life Science Incorporated, Greensboro, NC). Due to the cellular density of tissue and the use of recombinant growth factors in SFEM, media were changed every day for the duration of the study.

Characterizing Cell Response to Doxorubicin. K7M2, K12, and MC3T3 cells in monolayer, loaded in Matrigel or loaded in eBM, were cultured for 7 d with media changes every 1 to 2 d. Monolayer groups were seeded in 24-well plates at confluency and treated with 0 to 10 μM doxorubicin (Neta Scientific, Hainesport, NJ). Matrigel and eBM groups were treated with 0 to 1 μM doxorubicin. On day 7 for monolayer and Matrigel groups, media were collected, and metabolic activity was assessed with alamarBlue (Invitrogen). alamarBlue results were normalized to DNA content determined with the Quant-iT PicoGreen DNA Assay Kit (Invitrogen). For eBM groups, on days 1 and 7, eBM was prepared for flow cytometry and stained as described in *Flow Cytometry*. K7M2, K12, and MC3T3 cells were identified and quantified via flow cytometry as the CellTrace Yellow positive population.

Histology. eBM constructs were fixed in 4% paraformaldehyde, decalcified for 14 d in Calci-Clear (National Diagnostics, Atlanta, GA), and then paraffin-embedded and sectioned at 5 μm thickness. Sections were stained with H&E and MT. H&E slides were imaged with 10× and 20× objectives using a Nikon Eclipse TE2000U microscope and a Leica DMi8 microscope. For immunohistochemistry, OCN slides were rehydrated and exposed to enzyme-mediated antigen retrieval with Proteinase K at 37 °C for 30 min. Samples were then incubated in blocking buffer composed of 10% goat serum and 10 mg/mL Bovine Serum Albumin for 1 h at room temperature, after which they were incubated with recombinant anti-OCN antibody (ab93876, Abcam) at a concentration of 1:100 overnight at 4 °C. Slides were then treated with a secondary goat anti-rabbit antibody conjugated with AF488 (150081, Abcam) at a concentration of 1:100 for 1 h at room temperature. CD31 slides were rehydrated and exposed to heat-mediated antigen retrieval with sodium citrate buffer for 20 min. They were then incubated with recombinant anti-CD31 antibody (ab182981, Abcam) at a concentration of 1:250 for 1 h at room temperature. Slides were then treated with a secondary goat anti-rabbit antibody conjugated to AF488 (ab150081, Abcam) at a concentration of 1:300 for 1 h at room temperature. CD31 slides were counterstained with 5 μg/mL Lycopersicon esculentum (Tomato) lectin DyLight 649 (Vector Laboratories, Newark, CA) for 30 min at room temperature, and all slides were counterstained with DAPI (Thermo Fisher, Chicago, IL).

Flow Cytometry. eBM was dissociated via digestion at 37 °C with 1.5 mg/mL collagenase D and 1.5 U/mL Dispase II in 3% FBS in PBS for 3 h with gentle agitation. Resulting suspensions were filtered through a 100-μm filter to create a single-cell suspension, and progenitor cell and macrophage populations were characterized using flow cytometry (Attune NxT, Life Tech). Following Fcγ receptor blocking (1:40, TruStain FcX, BioLegend), cells were stained with antibodies. Progenitor cells were stained against hematopoietic lineage cocktail (1:5, eBioscience, #88-7772-72), Sca1 (1:333, eBioscience, #17-5981-82), cKIT (1:160, eBioscience, #47-1172-82), CD34 (1:50, eBioscience, #11-0341-82), and CD135 (1:20, eBioscience, #12-1351-82), as described (34). Macrophages were stained against F/480 (1:50, eBioscience #MF48021), CD86 (1:160, eBioscience #47-0862-82) and CD206 (1:40, eBioscience #48-2061-82). Cellular viability for both panels was evaluated with fixable Zombie Aqua (1:250, Life Tech). Macrophages with an M1 phenotype were characterized by F4/80+CD86+ populations and M2 phenotypes by F4/80+CD206+ populations.

Multiplex Proteomic Analysis. eBM-conditioned media were collected after 24 h of incubation with the constructs at day 1 and day 7. Media were frozen at −80 °C until measurement with a 36-plex ProcartaPlex Luminex panel (cat# EPXR360-26092-901, Thermo Fisher). Samples and kit were prepared and used as directed with samples incubated overnight in the refrigerator. The panel was detected on a Luminex 200 (Luminex, Austin, TX) and analyzed with Thermo Fisher software.

Bulk RNA-seq and Data Analysis. eBM was minced into cubes ≤0.5mm cubes and collected in 500 μL of TRIzol Reagent (Invitrogen). Samples were then homogenized with a Tissue-tearor (BioSpec, Bartlesville, OK) at the highest speed for 10 s intervals totaling 30 s, followed by sonication for another 10 s. Following RNA isolation, sequencing libraries were prepared using the Illumina Stranded mRNA Prep kit using the manufacturer's recommendations and then sequenced on an Illumina NextSeq 500 sequencer. RNA-seq data quality was checked using fastQC [https://www.bioinformatics.babraham.ac.uk/projects/fastqc/]. Subsequently, reads were mapped to the mouse genome (mm10) using STAR (66), and gene-level read counts were determined using "featureCounts" from Rsubread package (67). Differentially expressed genes were then identified using limma after voom normalization (68). Gene ontology/pathway enrichment analysis was performed using ToppGene (69). PCA plot and heatmaps were generated using R packages ggfortify and ggplot2, respectively. These data are publicly available on Dryad (DOI: 10.25338/B8693K) (70). We also reanalyzed a publicly available human OS dataset (GEO accession number: GSE99671) as described above and identified genes differentially expressed between OS and normal bone. Subsequently, we compared genes differentially expressed between eBM only and K7M2 to human OS RNA-seq to identify shared molecular mechanisms.

Statistical Analysis. Data are presented as mean ± SD. Statistical analysis was conducted with Prism 9.4.0 (GraphPad, San Diego, CA) software utilizing either unpaired *t* test assuming Gaussian distribution and one-way or two-way ANOVA with post hoc Tukey's test depending on the number of groups and comparisons. Groups with different letters indicate statistically significant differences ($P < 0.05$), while groups with the same letters are not significant. Each n represents eBM formed in different mice, with cranial and caudal locations equally represented, except where cranial and caudal comparisons are made directly.

Data, Materials, and Software Availability. RNA-seq data have been deposited in DRYAD (DOI: 10.25338/B8693K) (70). All study data are included in the article and/or *SI Appendix*.

ACKNOWLEDGMENTS. This work was supported in part by the UC Davis School of Veterinary Medicine Endowment Funds and Graduate Student Support Program to K.H.G. S.W.T. acknowledges financial support from the Musculoskeletal Tumor Society Mentored Research Award Project A23-0879. G.G.L. was in part supported by the UC Davis Comprehensive Cancer Center NIH P30 support grant 5P30CA093373-20. Part of the work was performed under the auspices of the

US Department of Energy by Lawrence Livermore National Laboratory under contract no DE-AC52-07NA27344. J.K.L. acknowledges financial support from the Lawrence J. Ellison Endowed Chair of Musculoskeletal Research. Schematics in this work were created using BioRender.

Author affiliations: [a]Department of Orthopaedic Surgery, University of California Davis Health, Sacramento, CA 95817; [b]School of Veterinary Medicine, University of California, Davis, CA 95616; [c]Physical and Life Sciences, Lawrence Livermore National Laboratory, Livermore, CA 94550; and [d]Department of Biomedical Engineering, University of California, Davis, CA 95616

1. B. R. Eaton *et al.*, Osteosarcoma. *Pediatr. Blood Cancer* **68**, e28352 (2021).
2. D. S. Geller, R. Gorlick, Osteosarcoma: A review of diagnosis, management, and treatment strategies. *Clin. Adv. Hematol. Oncol.* **8**, 705–718 (2010).
3. A. Luetke, P. A. Meyers, I. Lewis, H. Juergens, Osteosarcoma treatment–Where do we stand? A state of the art review. *Cancer Treat Rev.* **40**, 523–532 (2014).
4. A. Misaghi, A. Goldin, M. Awad, A. A. Kulidjian, Osteosarcoma: A comprehensive review. *SICOT J.* **4**, 12 (2018).
5. M. Cortini, N. Baldini, S. Avnet, New advances in the study of bone tumors: A lesson from the 3D environment. *Front. Physiol.* **10**, 814 (2019).
6. M. Gaebler *et al.*, Three-dimensional patient-derived in vitro sarcoma models: Promising tools for improving clinical tumor management. *Front. Oncol.* **7**, 203 (2017).
7. C. F. Monteiro, C. A. Custódio, J. F. Mano, Three-dimensional osteosarcoma models for advancing drug discovery and development. *Adv. Ther.* **2**, 1800108 (2019).
8. E. F. P. Peterse, T. N. van Leeuwen, A. M. Cleton-Jansen, In vitro studies of osteosarcoma: A researcher's perspective of quantity and quality. *J. Bone Oncol.* **7**, 29–31 (2017).
9. A. De Luca *et al.*, Relevance of 3d culture systems to study osteosarcoma environment. *J. Exp. Clin. Cancer Res.* **37**, 2 (2018).
10. Y. Zheng, G. Wang, R. Chen, Y. Hua, Z. Cai, Mesenchymal stem cells in the osteosarcoma microenvironment: their biological properties, influence on tumor growth, and therapeutic implications. *Stem. Cell Res. Ther.* **9**, 22–22 (2018).
11. Y. Suzuki, Y. Nishida, T. Naruse, T. Gemba, N. Ishiguro, Pericellular matrix formation alters the efficiency of intracellular uptake of oligonucleotides in osteosarcoma cells. *J. Surg. Res.* **152**, 148–156 (2009).
12. Y. Sun *et al.*, SFRP2 augments WNT16B signaling to promote therapeutic resistance in the damaged tumor microenvironment. *Oncogene* **35**, 4321–4334 (2016).
13. T. Tanaka *et al.*, Dynamic analysis of lung metastasis by mouse osteosarcoma LM8: VEGF is a candidate for anti-metastasis therapy. *Clin. Exp. Metastasis.* **30**, 369–379 (2013).
14. R. Elenjord *et al.*, Collagen I regulates matrix metalloproteinase-2 activation in osteosarcoma cells independent of S100A4. *FEBS J.* **276**, 5275–5286 (2009).
15. P. H. Tan, K. Z. Aung, S. L. Toh, J. C. Goh, S. S. Nathan, Three-dimensional porous silk tumor constructs in the approximation of in vivo osteosarcoma physiology. *Biomaterials* **32**, 6131–6137 (2011).
16. M. Rimann *et al.*, An in vitro osteosarcoma 3D microtissue model for drug development. *J. Biotechnol.* **189**, 129–135 (2014).
17. G. Bassi *et al.*, Scaffold-based 3D cellular models mimicking the heterogeneity of osteosarcoma stem cell niche. *Sci. Rep.* **10**, 22294 (2020).
18. M. Pavlou *et al.*, Osteomimetic matrix components alter cell migration and drug response in a 3D tumour-engineered osteosarcoma model. *Acta Biomater.* **96**, 247–257 (2019).
19. F. E. Freeman, R. Burdis, O. R. Mahon, D. J. Kelly, N. Artzi, A spheroid model of early and late-stage osteosarcoma mimicking the divergent relationship between tumor elimination and bone regeneration. *Adv. Healthc. Mater.* **11**, e2101296 (2022).
20. P. Indovina, G. Rainaldi, M. T. Santini, Hypoxia increases adhesion and spreading of MG-63 three-dimensional tumor spheroids. *Anticancer Res.* **28**, 1013–1022 (2008).
21. R. Rubio *et al.*, Bone environment is essential for osteosarcoma development from transformed mesenchymal stem cells. *Stem. Cells* **32**, 1136–1148 (2014).
22. E. C. Gonzalez Diaz *et al.*, A 3D osteosarcoma model with bone-mimicking cues reveals a critical role of bone mineral and informs drug discovery. *Adv. Healthc. Mater.* **11**, e2200768 (2022).
23. F. He *et al.*, Hydroxyapatite mineral enhances malignant potential in a tissue-engineered model of ductal carcinoma in situ (DCIS). *Biomaterials* **224**, 119489 (2019).
24. H. Chaddad *et al.*, Combining 2D angiogenesis and 3D osteosarcoma microtissues to improve vascularization. *Exp. Cell Res.* **360**, 138–145 (2017).
25. P. H. Tan, S. S. Chia, S. L. Toh, J. C. Goh, S. S. Nathan, The dominant role of IL-8 as an angiogenic driver in a three-dimensional physiological tumor construct for drug testing. *Tissue Eng. Part A* **20**, 1758–1766 (2014).
26. B. Kundu *et al.*, Mechanical property of hydrogels and the presence of adipose stem cells in tumor atroma affect spheroid formation in the 3D osteosarcoma model. *ACS Appl. Mater. Interfaces* **11**, 14548–14559 (2019).
27. C. F. Monteiro, C. A. Custodio, J. F. Mano, Bioengineering a humanized 3D tri-culture osteosarcoma model to assess tumor invasiveness and therapy response. *Acta Biomater.* **134**, 204–214 (2021).
28. C. Khanna *et al.*, An orthotopic model of murine osteosarcoma with clonally related variants differing in pulmonary metastatic potential. *Clin. Exp. Metastasis.* **18**, 261–271 (2000).
29. S. Crnalic, I. Hakansson, L. Boquist, R. Lofvenberg, L. A. Brostrom, A novel spontaneous metastasis model of human osteosarcoma developed using orthotopic transplantation of intact tumor tissue into tibia of nude mice. *Clin. Exp. Metastasis.* **15**, 164–172 (1997).
30. O. Berlin *et al.*, Development of a novel spontaneous metastasis model of human osteosarcoma transplanted orthotopically into bone of athymic mice. *Cancer Res.* **53**, 4890–4895 (1993).
31. C. Maloney *et al.*, Intratibial injection causes direct pulmonary seeding of osteosarcoma cells and is not a spontaneous model of metastasis: A mouse osteosarcoma model. *Clin. Orthop. Relat. Res.* **476**, 1514–1522 (2018).
32. T. Higuchi *et al.*, Osteosarcoma patient-derived orthotopic xenograft (PDOX) models used to identify novel and effective therapeutics: A review. *Anticancer Res.* **41**, 5865–5871 (2021).
33. C. Yang *et al.*, Bone microenvironment and osteosarcoma metastasis. *Int. J. Mol. Sci.* **21**, 6985 (2020).
34. Y. S. Torisawa *et al.*, Bone marrow-on-a-chip replicates hematopoietic niche physiology in vitro. *Nat. Methods* **11**, 663–669 (2014).
35. L. Ren *et al.*, Characterization of the metastatic phenotype of a panel of established osteosarcoma cells. *Oncotarget* **6**, 29469–29481 (2015).
36. C. Dumars *et al.*, Dysregulation of macrophage polarization is associated with the metastatic process in osteosarcoma. *Oncotarget* **7**, 78343–78354 (2016).
37. S. Sousa, J. Maatta, The role of tumour-associated macrophages in bone metastasis. *J. Bone Oncol.* **5**, 135–138 (2016).
38. S. S. Withers *et al.*, Association of macrophage and lymphocyte infiltration with outcome in canine osteosarcoma. *Vet. Comp. Oncol.* **17**, 49–60 (2019).
39. C. C. Kappel, M. C. Velez-Yanguas, S. Hirschfeld, L. J. Helman, Human osteosarcoma cell lines are dependent on insulin-like growth factor I for in vitro growth. *Cancer Res.* **54**, 2803–2807 (1994).
40. H. Y. Li *et al.*, Celastrol induces apoptosis and autophagy via the ROS/JNK signaling pathway in human osteosarcoma cells: An in vitro and in vivo study. *Cell Death Dis.* **6**, e1604 (2015).
41. J. H. Pahl *et al.*, Macrophages inhibit human osteosarcoma cell growth after activation with the bacterial cell wall derivative liposomal muramyl tripeptide in combination with interferon-gamma. *J. Exp. Clin. Cancer Res.* **33**, 27 (2014).
42. K. Yan *et al.*, MicroRNA-34a inhibits the proliferation and metastasis of osteosarcoma cells both in vitro and in vivo. *PloS One* **7**, e33778 (2012).
43. D. Saleiro, L. C. Platanias, Interferon signaling in cancer. Non-canonical pathways and control of intracellular immune checkpoints. *Semin. Immunol.* **43**, 101299 (2019).
44. H. Strander, Interferons and osteosarcoma. *Cytokine Growth Factor Rev.* **18**, 373–380 (2007).
45. A. Alfranca *et al.*, Bone microenvironment signals in osteosarcoma development. *Cell Mol. Life Sci.* **72**, 3097–3113 (2015).
46. X. D. Ho *et al.*, Whole transcriptome analysis identifies differentially regulated networks between osteosarcoma and normal bone samples. *Exp. Biol. Med. (Maywood)* **242**, 1802–1811 (2017).
47. A. Roguin, I. Kasis, M. W. Ben-Arush, R. Sharon, M. Berant, Fever and neutropenia in children with malignant disease. *Pediatr. Hematol. Oncol.* **13**, 503–510 (1996).
48. M. H. Cheng *et al.*, Piscidin-1 induces apoptosis via mitochondrial reactive oxygen species-regulated mitochondrial dysfunction in human osteosarcoma cells. *Sci. Rep.* **10**, 5045 (2020).
49. A. Costa, A. Scholer-Dahirel, F. Mechta-Grigoriou, The role of reactive oxygen species and metabolism on cancer cells and their microenvironment. *Semin. Cancer Biol.* **25**, 23–32 (2014).
50. W. Liu *et al.*, Characterizing the tumor microenvironment at the single-cell level reveals a novel immune evasion mechanism in osteosarcoma. *Bone Res.* **11**, 4 (2023).
51. M. Kansara *et al.*, Infiltrating myeloid cells drive osteosarcoma progression via GRM4 regulation of IL23. *Cancer Discov.* **9**, 1511–1519 (2019).
52. J. Cui, D. Dean, F. J. Hornicek, Z. Chen, Z. Duan, The role of extracelluar matrix in osteosarcoma progression and metastasis. *J. Exp. Clin. Cancer Res.* **39**, 178 (2020).
53. B. Zhang *et al.*, Hypoxia-inducible factor-1 promotes cancer progression through activating AKT/Cyclin D1 signaling pathway in osteosarcoma. *Biomed. Pharmacother.* **105**, 1–9 (2018).
54. A. Singla *et al.*, Wnt signaling in osteosarcoma. *Adv. Exp. Med. Biol.* **1258**, 125–139 (2020).
55. M. Katoh, Canonical and non-canonical WNT signaling in cancer stem cells and their niches: Cellular heterogeneity, omics reprogramming, targeted therapy and tumor plasticity (Review). *Int. J. Oncol.* **51**, 1357–1369 (2017).
56. M. R. Urist, Bone: Formation by autoinduction. *Science* **150**, 893–899 (1965).
57. C. Huggins, S. Wiseman, A. H. Reddi, Transformation of fibroblasts by allogeneic and xenogeneic transplants of demineralized tooth and bone. *J. Exp. Med.* **132**, 1250–1258 (1970).
58. V. Damerell, M. S. Pepper, S. Prince, Molecular mechanisms underpinning sarcomas and implications for current and future therapy. *Signal Transduct. Target Ther.* **6**, 246 (2021).
59. A. D. Waldman, J. M. Fritz, M. J. Lenardo, A guide to cancer immunotherapy: From T cell basic science to clinical practice. *Nat. Rev. Immunol.* **20**, 651–668 (2020).
60. J. Munoz-Garcia *et al.*, In vitro three-dimensional cell cultures for bone sarcomas. *J. Bone. Oncol.* **30**, 100379 (2021).
61. N. Takahashi, N. Udagawa, S. Tanaka, T. Suda, Generating murine osteoclasts from bone marrow. *Methods Mol. Med.* **80**, 129–144 (2003).
62. S. Simpson *et al.*, Comparative review of human and canine osteosarcoma: Morphology, epidemiology, prognosis, treatment and genetics. *Acta Vet. Scand.* **59**, 71 (2017).
63. E. A. Brooks *et al.*, Applicability of drug response metrics for cancer studies using biomaterials. *Philos. Trans. R Soc. Lond. B Biol. Sci.* **374**, 20180226 (2019).
64. C. E. Vorwald, K. C. Murphy, J. K. Leach, Restoring vasculogenic potential of endothelial cells from diabetic patients through spheroid formation. *Cell Mol. Bioeng.* **11**, 267–278 (2018).
65. G. Y. Lee, P. A. Kenny, E. H. Lee, M. J. Bissell, Three-dimensional culture models of normal and malignant breast epithelial cells. *Nat. Methods* **4**, 359–365 (2007).
66. A. Dobin, T. R. Gingeras, Mapping RNA-seq reads with STAR. *Curr. Protoc. Bioinformatics.* **51**, 11.14.11–11.14.19 (2015).
67. Y. Liao, G. K. Smyth, W. Shi, featureCounts: An efficient general purpose program for assigning sequence reads to genomic features. *Bioinformatics* **30**, 923–930 (2014).
68. C. W. Law, Y. Chen, W. Shi, G. K. Smyth, voom: Precision weights unlock linear model analysis tools for RNA-seq read counts. *Genome Biol.* **15**, R29 (2014).
69. J. Chen, E. E. Bardes, B. J. Aronow, A. G. Jegga, ToppGene Suite for gene list enrichment analysis and candidate gene prioritization. *Nucleic Acids Res.* **37**, W305–W311 (2009).
70. K. H. Griffin *et al.*, RNA-seq data. *Dryad*. https://doi.org/10.25338/B8693K. Accessed 16 August 2023.